

Review

High Performance Negative Dielectric Anisotropy Liquid Crystals for Display Applications

Yuan Chen ¹, Fenglin Peng ¹, Takashi Yamaguchi ², Xiaolong Song ³ and Shin-Tson Wu ^{1,*}

¹ CREOL, The College of Optics and Photonics, University of Central Florida, 4000 Central Florida Blvd, Orlando, FL 32816, USA; E-Mails: yuanucf@knights.ucf.edu (Y.C.); fenglin@knights.ucf.edu (F.P.)

² JNC, Petrochemical Corporation, Ichihara Research Center, Ichihara, Chiba 290-8551, Japan; E-Mail: y.haseba@jnc-corp.co.jp

³ Jiangsu Hecheng Display Technology Company, Nanjing 210014, China; E-Mail: song@hcch.net.cn

* Author to whom correspondence should be addressed; E-Mail: swu@ucf.edu; Tel.: +1-407-823-4763; Fax: +1-407-823-6880.

Received: 8 July 2013; in revised form: 21 August 2013 / Accepted: 26 August 2013 /

Published: 3 September 2013

Abstract: We review recent progress in the development of high birefringence ($\Delta n \geq 0.12$) negative dielectric anisotropy ($\Delta\epsilon < 0$) liquid crystals (LCs) for direct-view and projection displays. For mobile displays, our UCF-N2 (low viscosity, negative $\Delta\epsilon$, high Δn) based homogeneous alignment fringe-field switching (called n-FFS) mode exhibits superior performance to p-FFS in transmittance, single gamma curve, cell gap insensitivity, and negligible flexoelectric effect. For projection displays using a vertical alignment liquid-crystal-on-silicon (VA LCOS), our high birefringence UCF-N3 mixture enables a submillisecond gray-to-gray response time, which is essential for color sequential displays without noticeable color breakup. Our low viscosity UCF-N2 also enables multi-domain VA displays to use a thinner cell gap for achieving faster response time.

Keywords: liquid crystal display; negative dielectric anisotropy; fringe-field switching; projection displays

1. Introduction

Negative dielectric anisotropy ($\Delta\epsilon = \epsilon_{//} - \epsilon_{\perp} < 0$) liquid crystals (LCs) [1,2], in which the parallel permittivity ($\epsilon_{//}$) is smaller than the perpendicular one (ϵ_{\perp}), have been widely used for direct-view and projection displays. The common feature of a negative $\Delta\epsilon$ LC is that lateral polar substituents induce a dipole moment perpendicular to the principal molecular axis [3–5]. As described in [6], there are several approaches to induce polarity perpendicular to the molecular axis, such as (i) using certain polar linking groups (e.g., ester); (ii) adding a polar unit at an axial position of a cyclohexane ring; (iii) positioning polar unit(s) in lateral positions of an aromatic ring; and (iv) using heterocyclic rings with the heteroatom off-axis. However, the off-axis polar group would decrease the aspect ratio of the cylindrical molecular shape and hence tend to disturb the liquid crystal phase stability. Furthermore, the magnitude of the $\Delta\epsilon$ value will generally be much smaller than that of a positive $\Delta\epsilon$ LC. To use multiple polar groups to enhance $\Delta\epsilon$ often causes solubility problems or increases the rotational viscosity. Different off-axis polar groups, such as cyano and fluoro, have been employed to enlarge perpendicular dipole moment. To avoid image flickering [7], high resistivity is another crucial requirement for obtaining a high voltage-holding-ratio for active matrix liquid crystal displays (LCDs). A sufficiently large $\Delta\epsilon$ helps to lower the driving voltage, which in turn lowers the power consumption of a mobile display. Fluoro group provides an excellent resistivity [8], modest dipole moment, and low viscosity. Laterally fluorinated liquid crystals [9], *i.e.*, (2,3) difluorinated biphenyl, terphenyl [10] and tolane [11] usually exhibit a high resistivity and a modest $\Delta\epsilon$.

Most nematic LC devices require surface alignment layers in order to realize their useful electro-optic effect. However, some exceptions exist; for example, without any alignment layer polymer-stabilized blue phase with a negative $\Delta\epsilon$ LC host has been demonstrated recently to possess a negative Kerr constant and submillisecond response time [12]. A negative $\Delta\epsilon$ LC can be used in homogeneous alignment or vertical alignment (VA), depending on the electric field direction. In an in-plane switching (IPS) cell [13,14] or fringe-field switching (FFS) cell [15–17], the electric field is mainly in the lateral direction, while in a VA cell [18,19] or multi-domain VA (MVA) cell [20,21], the field is basically in the longitudinal direction. For mobile displays, IPS or FFS is a favored choice because they are more robust to external pressure, which is crucial for touch panels. In comparison with IPS, FFS mode has narrower electrode width and gap to eliminate dead zones so that its optical throughput is higher. Moreover, the capacitor formed by the passivation layer between the pixel and common electrode acts as a storage capacitance. As a result, FFS mode enables a larger aperture ratio, which translates into higher optical efficiency. Recently, it is found that the FFS mode with a negative $\Delta\epsilon$ LC (n-FFS) exhibits several advantages over its p-FFS (FFS mode using a positive $\Delta\epsilon$ LC) counterpart in higher transmittance, single gamma curve, cell gap insensitivity, and weaker flexoelectric effect [16]. A single-domain VA cell has been employed in liquid-crystal-on-silicon (LCOS) for data projectors because of its unprecedented contrast ratio [22], while MVA is a common choice for wide-view LCD TVs. In this paper, we will review recent progress on the negative $\Delta\epsilon$ and high Δn LC development for mobile displays using FFS mode, projection displays using VA LCOS, and wide-view LCD TVs using MVA. Among these applications, fast response time is a common requirement.

2. Response Time of Negative $\Delta\epsilon$ LCs

Fast response time plays a key role for reducing the image blur and improving transmittance in conventional LCDs, and for realizing color sequential displays without color breakup. The dynamic response of LC directors is governed by Ericksen-Leslie equation. Under single elastic constant and small angle approximations, Ericksen-Leslie equation can be simplified as [23]:

$$K_{ii} \frac{\partial^2 \phi}{\partial Z^2} + \Delta\epsilon E^2 \sin \phi \cos \phi = \gamma_1 \frac{\partial \phi}{\partial t} \quad (1)$$

where $\phi(Z,t)$ is the deformed angle of the LC directors, E is the applied electric field, γ_1 is the rotational viscosity of the LC, and K_{ii} is the elastic constant corresponding to the LC alignment. For a negative $\Delta\epsilon$ LC in IPS or FFS cell, the electric field mainly induces twist deformation [14,16]. Thus, K_{ii} can be approximated by K_{22} (twist elastic constant) [24]. On the other hand, in a VA cell K_{ii} is generally a weighted average of K_{11} (splay elastic constant) and K_{33} (bend elastic constant) [19]. However, under small angle approximation, K_{33} dominates and the contribution of K_{11} can be ignored. The rising process of LC directors can be accelerated by applying a high voltage for a short time, which is called overdrive method [25,26]. Meanwhile, during the decay period, if the holding voltage is close to threshold voltage (V_{th}), the decay time will be very slow. To speed up this relaxation process, the voltage can be turned off for a short period and then a small holding voltage is applied to keep the LC at the desired gray level; this is known as undershoot method [27]. However, the free relaxation time is intrinsically dependent on the LC properties and cell configuration. By substituting $E = 0$ into Equation (1), we can obtain the equation for the free relaxation process:

$$K_{ii} \frac{\partial^2 \phi}{\partial Z^2} = \gamma_1 \frac{\partial \phi}{\partial t} \quad (2)$$

By solving Equation (2), we obtain the free relaxation time of the LC directors:

$$\tau_{decay} = \frac{\gamma_1 d^2}{K_{ii} \pi^2} \quad (3)$$

where d is the cell gap. Based on Equation (3), the response time of an FFS or VA cell is proportional to the visco-elastic coefficient (γ_1/K_{ii}) of the LC material employed and d^2 . A thin cell gap would help to reduce the response time effectively. However, to maintain adequate phase retardation with reduced cell gap, a higher Δn LC is required. The LC birefringence is governed primarily by the molecular conjugation. The most effective approach for increasing Δn is to elongate the π -electron conjugation of the LC compounds [28–30]. Conjugation length can be extended by adding either unsaturated bonds (such as carbon-carbon triple bond) or phenyl rings to the rigid core structure. Due to insufficient photostability of carbon-carbon double bonds and triple bonds, conjugated phenyl rings are the preferred choices for obtaining high birefringence. However, using too many phenyl rings would cause two undesirable drawbacks: (1) its melting point and heat fusion enthalpy would increase, leading to a limited solubility; and (2) its viscosity would increase dramatically, resulting in a slower response time. Therefore, terphenyl [31] could be the optimal structure for thin-cell-gap VA LCOS. However, for FFS or MVA the required $d\Delta n$ is about 330–360 nm. If the cell gap is 3–4 μm , then $\Delta n \approx 0.09$ – 0.12 . Many

biphenyl compounds can meet this Δn requirement, but how to optimize the tradeoff between high $\Delta\epsilon$ for low voltage and low viscosity for fast response time remains a challenge.

3. Negative $\Delta\epsilon$ LCs for FFS Mode

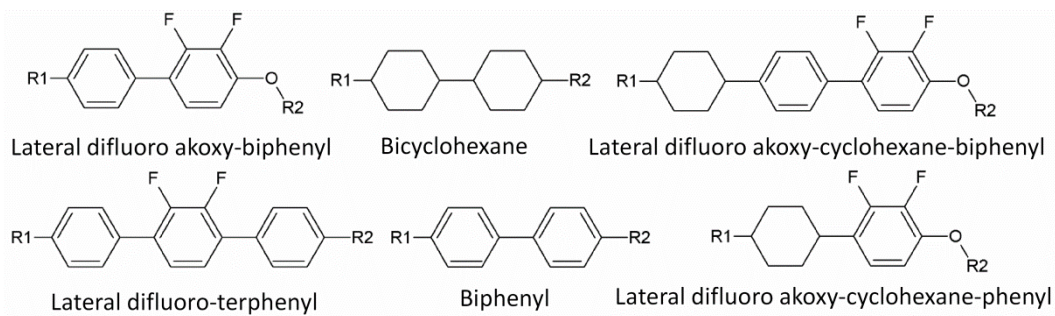
FFS [15,32,33] mode has been widely used for mobile displays, such as smartphones and tablet computers. Low power consumption for long battery life, wide viewing angle for multiple observers, high resolution for Retina display, and pressure-resistance for touch screen are the key requirements. In FFS mode, the electric field-induced molecular reorientation takes place mainly in the horizontal direction. Presently, most FFS LCDs use positive $\Delta\epsilon$ LCs. The primary reason is that it is relatively easy to obtain a large $\Delta\epsilon$ (~ 10) LC while keeping a low viscosity. Large $\Delta\epsilon$ helps to reduce operation voltage while low viscosity helps to shorten response time. However, p-FFS has some problems: (1) its peak transmittance is $\sim 88\%$; (2) the voltage-dependent transmittance (VT) curves do not overlap well for RGB colors, thus three gamma curves are required, which increases the complexity of driving electronics; (3) the VT curves are sensitive to the cell gap; and (4) a small but noticeable image flickering due to splay- and bend-induced flexoelectric effect [34,35].

To overcome these problems, recently we reported a n-FFS mode using a high performance negative $\Delta\epsilon$ LC [16]. The n-FFS mode has been investigated previously [13,15,17], but mainly by simulations. In this section, we compare the results of four different negative $\Delta\epsilon$ LC mixtures with relatively high Δn and low viscosity. The phase retardation effect on peak transmittance and on-state voltage is also investigated.

3.1. Low Viscosity Negative $\Delta\epsilon$ LCs

For high yield manufacturing, it is desirable to keep the cell gap above 3 μm . Thus, the required Δn is around 0.12. Previously we reported a high performance n-FFS with UCF-N1 [16], consisting of 60 wt % MLC-6882, 18% lateral difluoro akoxo-biphenyl, 17% lateral difluoro akoxo-cyclohexane-biphenyl [9] and 5% bicyclohexane compounds. The chemical structures are shown in Figure 1. We compare our results with MLC-6882 and a virtual positive $\Delta\epsilon$ LC (UCF-P1) whose $\Delta\epsilon = 10$ and other properties are the same as UCF-N1.

In addition to MLC 6882, UCF-N1 and UCF-P1, Table 1 includes three new negative $\Delta\epsilon$ LCs to be considered for FFS mode: HAV (HAV-634117, HCCH, Nanjing, China), ZOC (ZOC-7003, JNC, Ichihara, Japan), and UCF-N2. From Table 1, JNC ZOC has the lowest visco-elastic coefficient γ_1/K_{33} , but its $\Delta n \sim 0.1$ which is slightly too small. For an LCOS, the panel size is small, thus a submicron cell gap can be controlled without too much difficulty. However, a high Δn LC is needed to maintain $d\Delta n \sim 165$ nm. To obtain high Δn , we first formulated a binary LC mixture (M1) with two lateral difluoro-terphenyl homologs: R1 = 2, R2 = 4 (35 wt %) and R1 = 3, R2 = 5 (65 wt %) [36]. The general chemical structure is also shown in Figure 1. Its physical properties are: $\Delta n = 0.235$ (at $\lambda = 633$ nm and $T \sim 22$ °C), $\Delta\epsilon = -1.8$ and clearing temperature $T_c \sim 112.3$ °C. Next, we doped 10% M1 and 5% biphenyls to ZOC-7003. The final mixture is denoted as UCF-N2. Table 1 lists the physical properties of the six LC mixtures studied. The dielectric anisotropy was determined by measuring the capacitance of a homogeneous cell and a homeotropic LC cell [37,38].

Figure 1. Chemical structures of the liquid crystal (LC) compounds studied.**Table 1.** Physical properties of the LCs studied ($\lambda = 633$ nm, $T \sim 22$ °C and $f = 1$ kHz).

LC Mixture	T_c (°C)	Δn (633 nm)	Δn (550 nm)	γ_1/K_{33} (ms/ μm^2)	γ_1 (mPas)	$\Delta\epsilon$
MLC 6882	69	0.097	0.098	8.44	108	-3.1
UCF-N1	73.3	0.116	0.119	9.06	122.8	-3.82
UCF-P1	73.3	0.116	0.119	9.06	122.8	10
HAV	89.5	0.108	0.110	6.97	98.53	-3.79
ZOC	79	0.101	0.103	5.60	93.34	-4.36
UCF-N2	75	0.112	0.117	6.00	94.71	-3.77

We evaluated birefringence by measuring the phase retardation of a VA cell sandwiched between two crossed polarizers [39]. The VA cell has strong anchoring energy and cell gap $d \sim 9$ μm . A 1 kHz square-wave AC voltage signal was applied to the LC cell. A He-Ne laser ($\lambda = 633$ nm) and a tunable Argon ion laser ($\lambda = 457$ nm, 488 nm and 514 nm) were used as probing beams. The Δn of UCF-N1, HAV, ZOC and UCF-N2 was measured from 22 °C (RT) to a temperature close to T_c . Results are plotted in Figure 2. Dots represent the measured data and solid lines are the fitting curves using Haller's semi-empirical equation [40]:

$$\Delta n = \Delta n_0 (1 - T / T_c)^\beta \quad (4)$$

where Δn_0 is the extrapolated birefringence at $T = 0$ K and β is a material constant. At RT and $\lambda = 633$ nm, the Δn of ZOC, HAV and UCF-N2 is 0.101, 0.108 and 0.112, respectively.

For a full color display, we need to know the birefringence at red, green and blue wavelengths. Figure 3 depicts the measured birefringence dispersion of UCF-N1, HAV, ZOC and UCF-N2. Dots represent measured data and solid lines are fitting curves using the single-band birefringence dispersion model [41]:

$$\Delta n = G \lambda^2 \lambda^{*2} / (\lambda^2 - \lambda^{*2}) \quad (5)$$

where G is a proportionality constant and λ^* is the average resonant wavelength of the LC mixture. Through fitting, we obtained $G = 2.10 \mu\text{m}^{-2}$, $2.57 \mu\text{m}^{-2}$, $3.40 \mu\text{m}^{-2}$ and $2.13 \mu\text{m}^{-2}$ and $\lambda^* = 218.4$ nm, 194.6 nm, 165.7 nm and 215.8 nm for UCF-N1, HAV, ZOC and UCF-N2, respectively. With a higher Δn , UCF-N1 and UCF-N2 have a longer resonant wavelength as expected. With these fitting parameters, we can calculate the birefringence at a desired wavelength through Equation (5).

Figure 2. Temperature dependent Δn of UCF-N1, HAV, ZOC and UCF-N2 at $\lambda = 633$ nm.

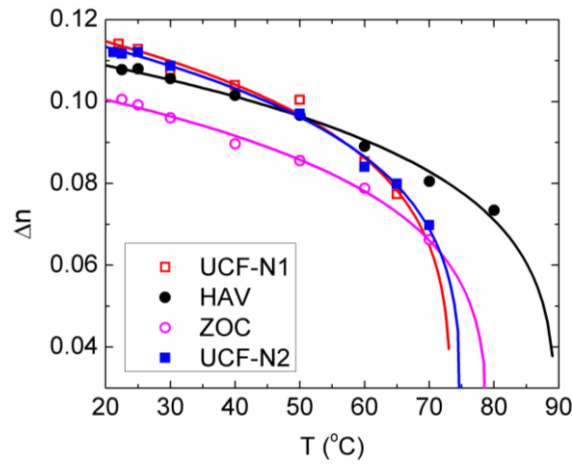
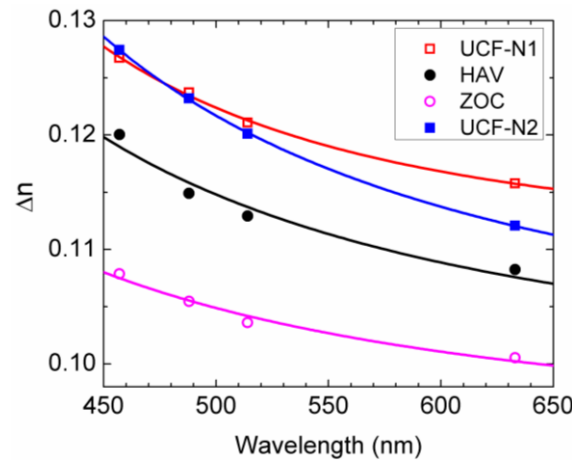


Figure 3. Birefringence dispersion of the four LC mixtures studied.



From the relaxation time measurement of the VA cell, we can obtain γ_1/K_{33} [38]. We measured γ_1/K_{33} at different temperatures and fitted the experimental results with Equation (6), as shown in Figure 4a:

$$\frac{\gamma_1}{K_{33}} = \frac{a \cdot \exp(E_a / K_B T)}{(1 - T / T_c)^\beta} \tag{6}$$

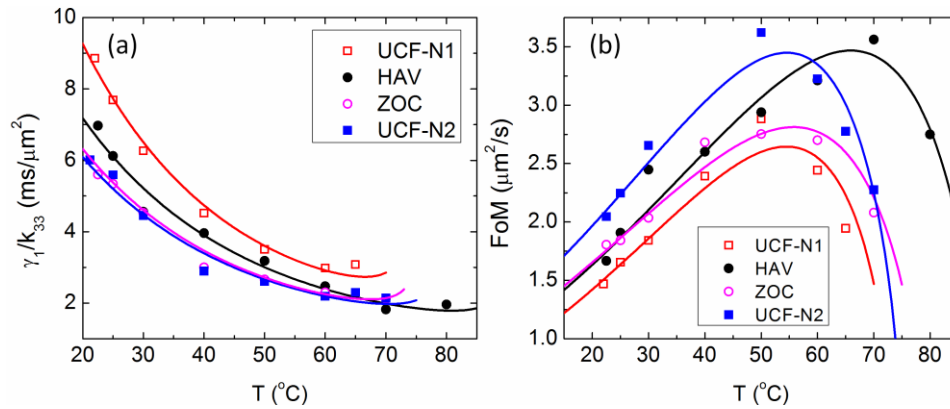
where a is a proportionality constant, E_a is the activation energy of the LC mixture, and K_B is the Boltzmann constant. Through fittings, we obtained $E_a = 279, 270.1, 260.7$ and 274.5 meV for UCF-N1, HAV, ZOC and UCF-N2, respectively. To compare the overall performance of these LCs we define a figure of merit as $FoM = (\Delta n)^2 / (\gamma_1 / K_{33})$. Since K_{33} and γ_1 are temperature dependent, we can rewrite FoM as follows [42]:

$$FoM = b(\Delta n_o)^2 \left(1 - \frac{T}{T_c}\right)^{3\beta} \exp\left(\frac{-E_a}{K_B T}\right) \tag{7}$$

where b is a proportionality constant. Figure 4b depicts the measured data and fitting curve based on Equation (7). Near RT, UCF-N2 possesses the highest FoM , hence the fastest response time for the same phase retardation. Indeed, as will be shown later, the calculated response time of an n-FFS cell

using UCF-N2 is 32% faster than that of UCF-N1. At 22 °C, the FoM of UCF-N2 is $2.05 \mu\text{m}^2/\text{s}$, and it increases to $3.62 \mu\text{m}^2/\text{s}$ at 50 °C. As the temperature increases, visco-elastic coefficient decreases more quickly than birefringence initially, resulting in an increased FoM . As T approaches T_c , Δn decreases more quickly than γ_1/K_{33} leading to a sharply declined FoM , as Figure 4b depicts. High T_c is also important for wide operating temperature range.

Figure 4. Temperature dependent (a) γ_1/K_{33} and (b) FoM of the four LCs studied.



3.2. Device Configuration

Next, we compare the electro-optic properties of n-FFS and p-FFS modes. We calculated the LC director distribution by a commercial LCD simulator DIMOS.2D and optical transmittance by extended Jones matrix [43]. As will be shown later, the preferred $d\Delta n$ value for achieving high transmittance at $\lambda = 550 \text{ nm}$ and fast response time is $\sim 360 \text{ nm}$ for n-FFS and $\sim 380 \text{ nm}$ for p-FFS. This difference originates from more efficient LC director reorientation in n-FFS. To make a fair comparison between n-FFS and p-FFS, we use the same electrode width $w = 2 \mu\text{m}$ and gap $l = 3 \mu\text{m}$, same pretilt angle (2°) but the rubbing angle is 10° and 80° respectively w.r.t. the horizontal axis, as shown in Figure 4a,b. The passivation layer between the pixel and common electrodes is SiO_x whose thickness is $d_p = 250 \text{ nm}$ and dielectric constant is $\epsilon_p = 4.5$ [44].

Figures 5c and 4d depict the simulated equal-potential lines and LC director deformation in a voltage-on state of n-FFS and p-FFS, respectively. The cell is sandwiched between two crossed linear polarizers, and the transmission axis of the bottom polarizer is parallel to the rubbing direction. Thus, the transmittance at a given position and voltage V can be expressed as [39,45]:

$$T/T_0 = \sin^2(2\Psi(V))\sin^2(\pi d\Delta n_{eff}(V)/\lambda) \tag{8}$$

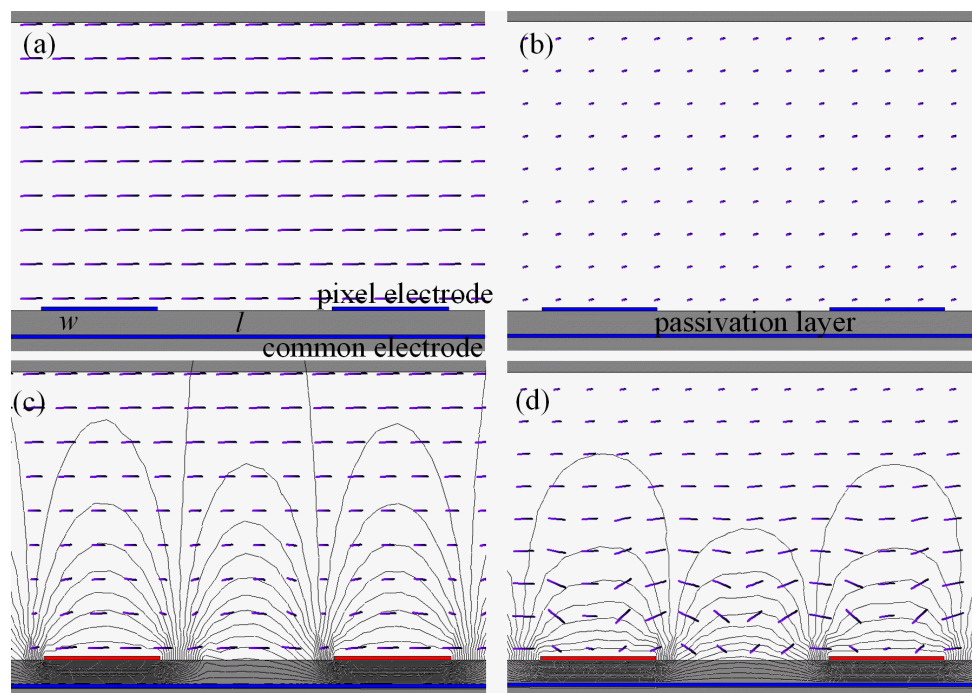
where $\Psi(V)$ is the voltage dependent azimuthal component of the angle between the polarizer and LC director's optic axis, T_0 is the transmitted light through parallel polarizers and Δn_{eff} is the effective birefringence of LC at voltage V and wavelength λ . Please note that the electric field in a FFS cell is not uniform spatially. So, the transmittance at each position as Equation (8) describes may not be the same. To calculate transmittance, we have to do the spatial averaging for each pixel. The dark state of a FFS cell happens when $V = 0$, and the transmittance reaches a maximum when the LC directors are reoriented by 45° .

3.3. Phase Retardation Effect

Both peak transmittance (T_p) and on-state voltage (V_{on}) are dependent on the phase retardation, or $d\Delta n/\lambda$ of the FFS cell. Figure 6 depicts the calculated T_p and V_{on} at different $d\Delta n/\lambda$ values for both n-FFS (with UCF-N1) and p-FFS (with UCF-P1). For n-FFS, as $d\Delta n/\lambda$ increases from 0.35 to 1.1, T_p climbs to a peak of 98.1% at $d\Delta n/\lambda \approx 0.67$ and then gradually decreases. Meanwhile, V_{on} decreases to a minimum at $d\Delta n/\lambda \approx 0.7$ and then bounces back. Since green light is the major component of white light, we optimize the cell gap at $\lambda = 550$ nm. Therefore, for n-FFS we choose $d\Delta n \sim 360$ nm for $\lambda = 550$ nm, in order to achieve high transmittance and fast response time. However, for p-FFS both T_p and V_{on} increase continuously in the $d\Delta n/\lambda$ range studied. The insufficient phase retardation results from the large tilt angle of the directors in the p-FFS (Figure 4b), because the positive $\Delta\epsilon$ LC directors tend to align parallel to the electric fields. Compromising the performance between transmittance, V_{on} and response time, we chose $d\Delta n \sim 380$ nm at $\lambda = 550$ nm as the optimal value for p-FFS.

An attractive feature of n-FFS can be found in Figure 5: in the $0.60 < d\Delta n/\lambda < 0.78$ range T_p keeps larger than 95% and V_{on} only varies slightly, which provides a reasonably large cell gap manufacturing tolerance. By contrast, in the same range the V_{on} of p-FFS climbs almost linearly from 4 V to 5.2 V and T_p increases from 82% to 91.7%. Although the T_p of p-FFS gradually saturates when $d\Delta n/\lambda > 0.7$, its V_{on} increases dramatically. High operation voltage leads to high power consumption.

Figure 5. Device configuration and initial director alignment in (a) n-FFS (fringe-field switching) and (b) p-FFS; Equal-potential lines and LC director deformation in the voltage-on state of (c) n-FFS and (d) p-FFS.



3.4. Wavelength Effect

To achieve high transmittance, we optimize the cell gap for $\lambda = 550$ nm. However, $d\Delta n/\lambda$ varies for RGB colors due to the change in λ and birefringence dispersion as Figure 3 depicts. As Equation (5)

indicates, a high birefringence LC is more dispersive in the visible region because of its longer λ^* . Thus, the phase retardation for blue will be larger than the optimized value for green, but smaller for red. Larger birefringence dispersion causes a larger deviation from the optimized phase retardation value and hence leads to a lower peak transmittance. To investigate the birefringence dispersion effect on the transmittance for RGB ($\lambda = 650, 550$ and 450 nm) colors, we calculated the VT curves of n-FFS with three exemplary LCs: UCF-N0, UCF-N1 and UCF-N3, as shown in Figure 7a–c. UCF-N0 is an imaginary material; it has identical properties as UCF-N1 but without dispersion, *i.e.*, its Δn is independent of wavelength. This represents an extreme case. On the other hand, UCF-N3 is a high birefringence negative $\Delta\epsilon$ LC we developed for VA LCOS (to be discussed in next session), whose $\Delta n = 0.177, 0.191$ and 0.214 at RGB colors, respectively. For all the n-FFS cells studied, we set $d\Delta n = 360$ nm. Therefore for UCF-N0, its $d\Delta n/\lambda = 0.55, 0.65$ and 0.80 for RGB, respectively. From Figure 6, we find the peak transmittance for RGB is $\sim 92\%, 98\%$ and 91% , which is consistent with the calculated VT curves of UCF-N0 for RGB colors, as depicted in Figure 7a. Moreover, both RGB colors have nearly the same V_{on} . The inset in Figure 7a depicts the normalized VT curves and they overlap amazingly well. Thus, a single gamma curve driving can be realized for n-FFS, which would simplify the driving circuit. This property holds true for UCF-N1 and UCF-N3 as well. From Figure 5, V_{on} is relatively insensitive to $d\Delta n/\lambda$ in the range of $0.55\text{--}0.90$. The peak transmittance of UCF-N1 reaches $\sim 98\%$ ($\lambda = 550$ nm) at $V_{on} = 4.6$ V. As the birefringence dispersion gets larger, $T_p(B)$ and $T_p(R)$ drop further to 85% and 89% for UCF-N1, respectively. For UCF-N3, $T_p(B)$ decreases to 71.3% , since $d\Delta n/\lambda$ deviates from the optimized value too much. $T_p(G)$ also drops slightly to 94% since the cell gap employed here is 1.89 μm , which is much smaller than the electrode width (3 μm). Fine electrode configuration [17] or adding chiral dopant [44] would help increase T_p for a thin-cell-gap FFS cell.

For comparison, we also calculate the VT curves of a p-FFS cell using UCF-P1 ($d = 3.19$ μm). Let's call it FFS-P1. As Figure 7d shows, the peak transmittance of RGB colors take place at different voltages. For 550 nm, T_p reaches $\sim 88\%$ at $V_{on} = 4.4$ V, and for 650 nm T_p reaches $\sim 78\%$ at $V_{on} = 4.0$ V. But for $\lambda = 450$ nm, T_p can reach 88.1% but at a much higher voltage (6.8 V). The inset in Figure 7d depicts the normalized VT curves. Obviously, they do not overlap well. Thus, three different gamma curves are needed to drive the RGB pixels.

Figure 6. T_p and V_{on} at different $d\Delta n/\lambda$ for n-FFS and p-FFS.

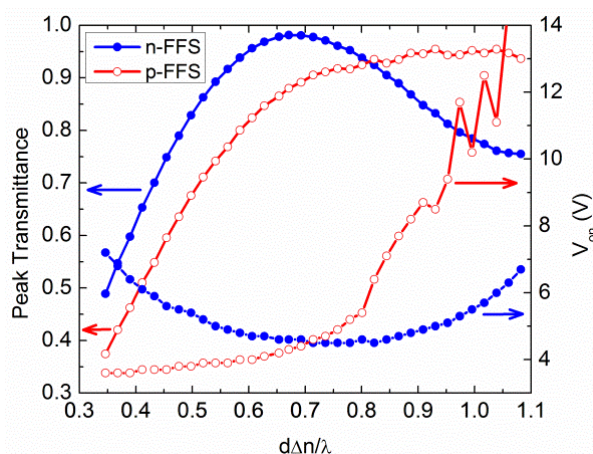
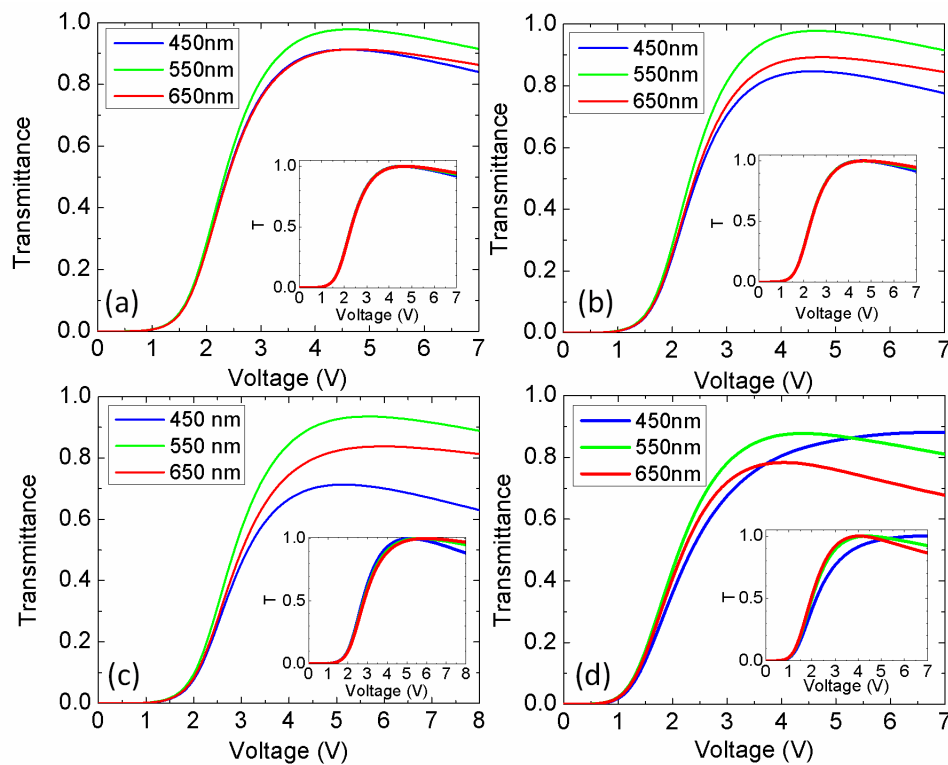


Figure 7. VT curves for FFS cell using (a) UCF-N0; (b) UCF-N1; (c) UCF-N3; and (d) UCF-P1 for RGB colors. Inset plots show the normalized VT curves.



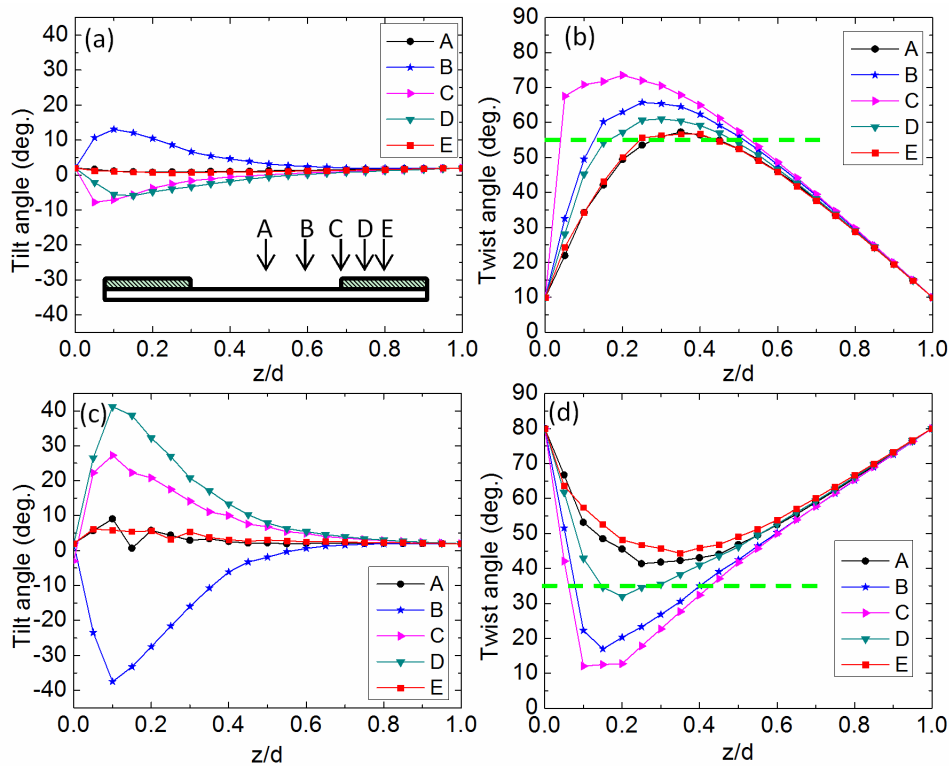
3.5. Director Deformation Distribution

In order to understand the differences between n-FFS and p-FFS modes, we study the LC tilt and twist angle distributions of FFS-N1 (n-FFS filled with UCF-N1) and FFS-P1 cells at five positions: A, B, C, D, and E as Figure 8a shows. Negative LCs tend to align perpendicular to the electric field, so the tilt angles at position A to E are relatively small, as shown in Figure 7a. To obtain maximum transmittance, ideally the twist angle should occur at 45° , as Equation (8) indicates. From Figure 8b, the LC directors are largely twisted near the bottom of the cell ($z/d < 0.4$) by the electric field and gradually reoriented back to the rubbing direction due to the strong anchoring force provided by the top surface. For FFS-N1, the maximum twist angle from the initial rubbing direction is around 46° at A and E. The tilt angle at A and E is close to 0° , which contributes effectively to the phase retardation. At B, C, and D, the horizontal electric field is stronger and the maximum twist angle is $\sim 55^\circ$. Meanwhile, the tilt angle at $z/d \sim 0.1$ is $\sim \pm 10^\circ$, which would slightly decrease the phase retardation and compensate the over twist. Moreover, the on-state of the n-FFS cell is like two cascaded TN cells [44] due to the small tilt angle. As a result, polarization rotation effect dominates and the color dispersion is suppressed.

In contrast, the maximum twist angle of FFS-P1 is either larger than 63° (B and C) or smaller than 38° (A and E), as Figure 7d depicts. The over- or under-twist leads to inefficient phase retardation. Only at position D, the maximum twist angle is about 48° , however the tilt angle is about 41° at $z/d = 0.1$. The large tilt angle (Figure 7c) caused by the strong vertical field dramatically decreases the effective birefringence and hence the peak transmittance. Meanwhile, with a large tilt angle at positions B, C, and D, the phase retardation effect (which is wavelength sensitive) becomes quite obvious, resulting in severe wavelength dispersion. In addition, from Figure 5d, splay and bend

deformation occurs and electric polarization is induced, which is known as flexoelectric effect [34]. The light transmittance would change slightly from negative to positive frames, resulting in a small image flickering. By contrast, this effect is negligible in n-FFS due to the small tilt angle.

Figure 8. Simulated tilt angle distribution of (a) FFS-N1 and (c) FFS-P1; Twist angle distribution of (b) FFS-N1 and (d) FFS-P1.



As Figure 7 shows, FFS-P1 has a lower threshold-like voltage (V_{th}) than FFS-N1 because its $\Delta\epsilon$ (+10) is much larger than that of UCF-N1 (-3.82), assuming their K_{22} is the same. However, the on-state voltage of FFS-P1 ($V_{on} \sim 4.4$ V) is nearly the same as that of FFS-N1 (4.6 V). This can be explained by the LC director distributions shown in Figure 8a–d. FFS-N1 has more efficient twist angle ($\sim 45^\circ$) and smaller tilt angle than FFS-P1 so that its effective birefringence is higher. As a result, a smaller voltage swing ($\Delta V = V_{on} - V_{th}$) is needed to reach the peak transmittance. Therefore, FFS-N1 has a comparable V_{on} to FFS-P1, although its $\Delta\epsilon$ is much smaller.

3.6. Low Operation Voltage

Low power consumption is highly desirable for a mobile display because it lengthens the battery life. The power consumption of a LCD comes from two parts: electronic and backlight. Generally speaking, the total power consumption is governed by the optical throughput of the panel, circuit frame rate, capacitance, and square of the operation voltage. For a given resolution and frame rate, the power consumption is closely related to the optical efficiency and operation voltage.

Several approaches have been considered for lowering V_{on} . From device side, we can decrease the rubbing angle [45,46]. The tradeoff is slower rise time, although the decay time remains almost the same. In FFS mode, the capacitor formed by the passivation layer between the pixel and common

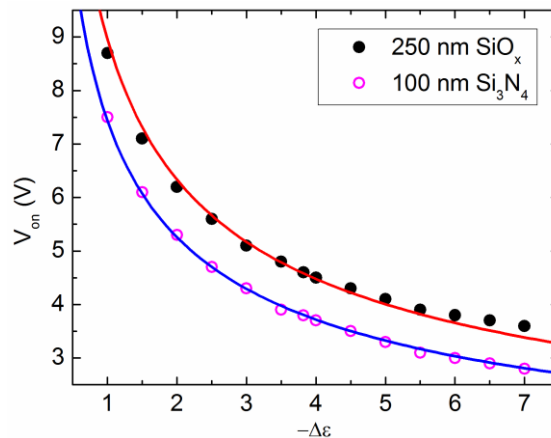
electrode acts as a storage capacitor ($C_s \sim \epsilon_p A_{pixel}/d_p$), which is in parallel to the LC capacitor. Therefore, we can use a thin and large ϵ_p dielectric layer to increase C_s and reduce the voltage shielding effect [47]. For example, if we reduce the SiO_x layer thickness from 250 nm to 100 nm, then V_{on} would decrease from 4.6 V to 3.9 V for FFS-N1. If we use 100 nm Si_3N_4 passivation layer ($\epsilon_p = 6.5$), then V_{on} would drop to 3.8 V. A tradeoff is the increased charging time resulting from the increased C_s . However, for a high resolution mobile display, its pixel size is small so that C_s can still be kept relatively small for quick addressing.

From material aspect, a straightforward way to reduce V_{on} is to increase $\Delta\epsilon$. As shown in Figure 9, as $\Delta\epsilon$ increases, the V_{on} of n-FFS decreases dramatically initially and then gradually saturates for both 250-nm SiO_x layer (solid circle) and 100-nm Si_3N_4 layer (open circle). The two sets of data points are well fitted by the following semi-empirical equation:

$$V_{on} = \alpha \cdot \pi \sqrt{\frac{K_{22}}{\epsilon_0 \Delta\epsilon}} \tag{9}$$

where α is a proportionality constant related to the device configuration (e.g., rubbing angle) and the passivation layer. From fittings, we obtained $\alpha = 3.40$ and 2.83 for the 250-nm SiO_x layer and 100-nm Si_3N_4 layer, respectively. Smaller α indicates less voltage shielding effect and more efficient driving. In Figure 8, the deviation in the large $\Delta\epsilon$ region originates from the larger dielectric constant mismatch between liquid crystal and SiO_x , which in turn shields the applied voltage. Two more tradeoffs of large $\Delta\epsilon$ are: (1) increased viscosity, which is undesirable for response time; and (2) increased ionic impurity which causes image sticking [48]. As Figure 8 shows, the reduction in V_{on} would gradually saturate. Thus, there is a delicate balance while selecting a large $\Delta\epsilon$ LC material for n-FFS.

Figure 9. $\Delta\epsilon$ effect on the V_{on} of n-FFS under two types of passivation layers.



3.7. Response Time

Both rise time and decay time are calculated between the 10% and 90% transmittance change. For FFS-P1 with $d = 3.19 \mu\text{m}$, the simulated [rise time, decay time] is [23.8 ms, 25.7 ms]. For the n-FFS cell with MLC-6882 ($d = 3.66 \mu\text{m}$ and $V_{on} = 4.5 \text{ V}$) the simulated [rise time, decay time] is [23.4 ms, 34.8 ms]. With our UCF-N1 ($d = 3.02 \mu\text{m}$), the calculated [rise time, decay time] is [16.2 ms, 24.1 ms]. Our UCF-N1 has faster response time than MLC-6882 because of its thinner cell gap. On the other

hand, UCF-N1 has faster response time than FFS-P1 due to its more uniform twist and tilt angles. A lower viscosity LC would further reduce the response time. For example, if we use a lower viscosity LC, such as UCF-N2, the calculated [rise time, decay time] decreases about 30% to [10.9 ms, 16.5 ms].

This response time is still 2X to 3X longer than that of the state-of-the-art MVA LCD TV. In MVA, the involved elastic constant is K_{33} , but in n-FFS it is K_{22} . For most nematic LCs, K_{33} is about 2X to 3X larger than K_{22} . Therefore, this could be an intrinsic disadvantage when comparing n-FFS with MVA for TV applications, where touch panel is not necessary. To further improve the response time for n-FFS, we need to develop lower viscosity negative $\Delta\epsilon$ LCs or use a thinner cell gap.

3.8. Summary

We have developed a low viscosity negative $\Delta\epsilon$ LC mixture (UCF-N2, $\gamma_1 = 94$ mPas and $\Delta n \sim 0.12$) for n-FFS with a 3- μm cell gap. Our n-FFS shows superior performances to p-FFS in following aspects: (1) higher transmittance (98% vs. 88%); (2) single gamma curve vs. 3 gamma curves for RGB pixels; (3) both on-state voltage and peak transmittance are less sensitive to cell gap variation, (4) faster response time due to a slightly thinner cell gap and more uniform LC twist and tilt angles, and (5) comparable on-state voltage to p-FFS although the LC mixture has a smaller $\Delta\epsilon$ (-3.8 vs. $+10$). Therefore, n-FFS has potential to replace p-FFS for next-generation mobile displays or even TV applications. Moreover, due to the homogeneous alignment and horizontal molecular orientation, n-FFS has intrinsic wide viewing angles. Various compensation films for FFS mode have been developed [49,50]. With one biaxial film, the 100:1 isocontrast contour can be achieved over the $\pm 80^\circ$ viewing zone [16]. To further widen the viewing angle, multi-domain structures can be considered [32].

4. Negative $\Delta\epsilon$ LCs for VA Mode

Two types of VA cells are discussed here: single domain VA LCOS for projection displays and multi-domain VA (MVA) for direct-view LCD TVs.

4.1. LCOS

Single domain VA has been extensively used in LCOS for projection displays because of its unprecedented contrast ratio (CR) [22]. To enable color sequential projection display [51–53], which requires only a single monochrome LCD panel so that the optical system is much simpler than that using three panels, fast response time (<1 ms) is critically needed in order to suppress color breakup. To achieve submillisecond response time, several approaches have been proposed, such as thin VA LCOS cell [18,19], mixed-mode twisted nematic (MTN) cell [54] and ferroelectric cell [55]. Among these methods, thin VA LCOS is attractive because of its high CR and fast response time, as shown in Equation (3). However, fringing field degrades the contrast ratio and reduces the display brightness [56]. A straightforward way to suppress fringing field effect is to reduce the cell gap. A major challenge for the thin cell approach is the need of a high birefringence and low viscosity LC. For a VA LCOS, the required $d\Delta n$ is ~ 165 nm (at $\lambda = 550$ nm) in order to achieve high reflectance at a low voltage (<5 V) [57].

In projection displays, high power arc lamp or LED lamp is commonly used as light source. Because of thermal effect, the LCOS panel is usually operated at 40–50 °C. As the temperature increases, both birefringence and visco-elastic coefficient decrease. The former vanishes at T_c . Therefore, it is important to design a LC with high T_c ($\gg 50$ °C). In an LCOS, the electric field is in the longitudinal direction. To realize the electro-optic effect of a VA cell, we need a negative $\Delta\epsilon$ LC. To achieve high resistivity, fluorinated LCs are commonly used as mentioned earlier [9]. However, some laterally difluoro high Δn compounds are difficult to align, especially at elevated temperatures [36]. A poor LC alignment leads to a low contrast ratio.

UV stability is another critical issue for a high Δn LC due to its relatively long conjugation length. In an LCOS projector, the arc lamp is relatively bright. Although filters are used to block the unwanted UV and infrared lights from the lamp, residual UV contents could still decompose the LC materials if the molecular structures are not intrinsically stable.

4.1.1. LC Material

In experiment, we prepared a mixture called UCF-N3 by doping 15.1 wt % lateral difluoro alkoxy-biphenyls, 8.9 wt % alkoxy-cyclohexane-phenyls, and 15.4 wt % alkoxy-cyclohexane-biphenyls [9,58], whose chemical structures are shown in Figure 1, into our M1 host in order to increase $\Delta\epsilon$ while keeping a low viscosity. An excellent dark state was achieved in the entire nematic range. The clearing point of UCF-N3 is $T_c \sim 93.2$ °C.

4.1.2. Physical Properties

We first measured the dielectric anisotropy of UCF-N3 at $f = 1$ kHz. Results are: $\Delta\epsilon = -3.74$ at 23 °C and -2.91 at 50 °C. Next, we measured the temperature dependent Δn of UCF-N3 at $\lambda = 633$ nm from 25 °C to 90 °C. Results are plotted in Figure 10a, where dots represent the measured data and solid line is the fitting curve using Equation (4). Through fitting, we obtained $\Delta n_0 = 0.265$ and $\beta = 0.177$.

To investigate the electro-optic performances at RGB colors, we measured the birefringence dispersion of UCF-N3 at 50 °C; the intended operation temperature for an LCOS projector. Results are shown in Figure 10b; here dots are the measured data and solid line represents fitting result using Equation (5). From fitting we obtained $G = 2.64\text{E-}6 \mu\text{m}^{-2}$ and $\lambda^* = 241.1$ nm. With higher Δn , UCF-N3 has a longer λ^* than the previously mentioned mixtures for FFS. With these parameters and through Equation (5), we can obtain the birefringence at any wavelength. For example, we find $\Delta n = 0.191$ at $\lambda = 550$ nm and 50 °C. Thus, for a VA LCOS we need $d = 0.93 \mu\text{m}$ to achieve $\sim 100\%$ reflectance (normalized to parallel polarizers) at a relatively low operating voltage (< 5 V). Although challenging, ferroelectric LCOS with $d \sim 0.8 \mu\text{m}$ has been commercialized.

We also measured the γ_1/K_{33} of UCF-N3 at different temperatures and fitted the experimental data with Equation (6), as shown in Figure 11a. Here the activation energy is $E_a = 286.9$ meV, which is larger than that of UCF-N2 developed for FFS. Usually higher birefringence involves longer conjugation length and hence higher viscosity, which leads to larger activation energy. To evaluate the overall performance of UCF-N3 at different temperatures, Figure 11b depicts the measured FoM data and fitting curve based on Equation (7). At room temperature, the FoM of UCF-N3 is $\sim 2.6 \mu\text{m}^2/\text{s}$, and it increases to $4.8 \mu\text{m}^2/\text{s}$ at 50 °C.

Figure 10. (a) Temperature dependent Δn of UCF-N3 at $\lambda = 633$ nm; (b) Wavelength dependent Δn of UCF-N3 at $T = 50$ °C.

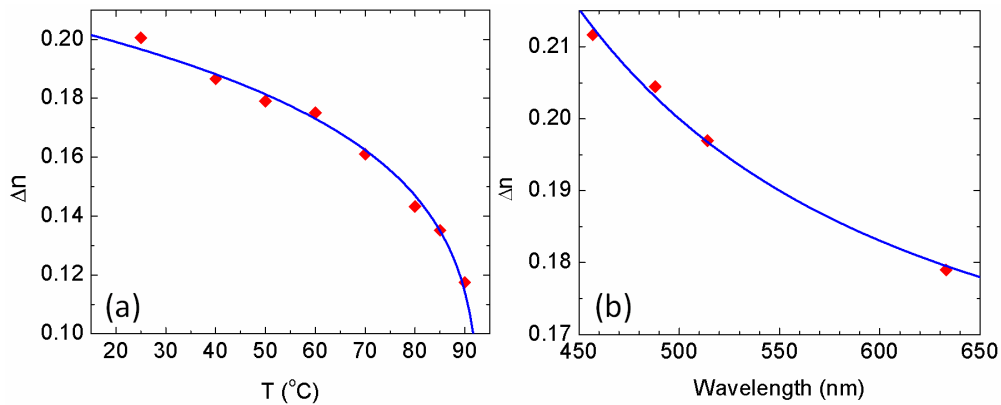
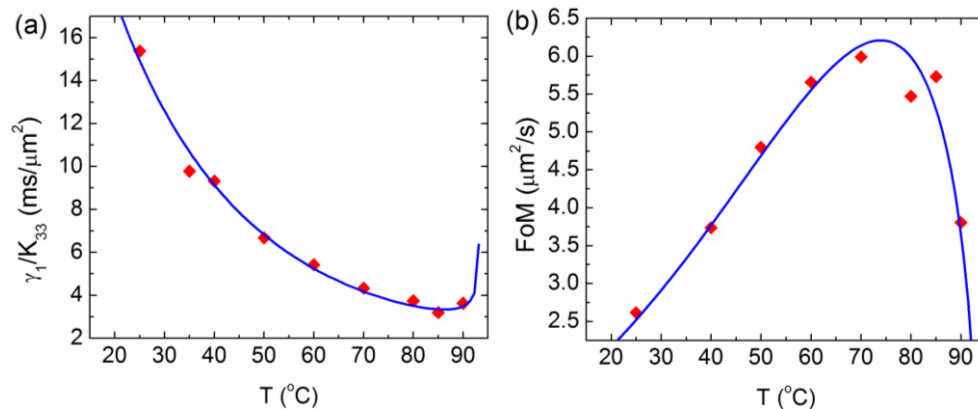


Figure 11. Temperature dependent (a) γ_1/K_{33} and (b) FoM of UCF-N3.



4.1.3. Simulation Results for VA LCOS

The electro-optical characteristics of UCF-N3 in a vertical alignment liquid-crystal-on-silicon (VA-LCOS) are calculated using a commercial LCD simulator DIMOS 2.0. In simulation, we used $d = 0.93$ μm , $\Delta n = 0.191$ at $\lambda = 550$ nm, and $\gamma_1/K_{33} \sim 6.7$ $\text{ms}/\mu\text{m}^2$ at $T = 50$ °C. The initial pretilt angle is 88° and the azimuthal angle is 45° w.r.t. the optic axis of the polarizing beam splitter (PBS). A reflector is placed on the inner surface of the VA cell. We calculated the voltage-dependent reflectance (VR) curves for RGB colors. As shown in Figure 12, for the green light the on-state voltage occurs at 4.83 V. The birefringence dispersion is relatively large for high birefringence LCs. As shown in Figure 10b, $\Delta n = 0.214, 0.191, 0.177$ at $\lambda = 450$ nm, 550 nm and 650 nm, respectively. The peak transmittance for RGB colors occur at different voltages. Thus, three gamma curves are needed for driving the RGB sub-frames.

We also calculated the gray-to-gray (GTG) response times of the VA LCOS, and results are summarized in Table 2. Taking green color as an example, the VR curve was uniformly divided into eight gray levels (1–8) and the response time between every two gray levels was calculated. Here both rise time and decay time are calculated between 10% and 90% reflectance change. From Table 2, we find the rise time is 0.26 ms and decay time is 0.40 ms between gray levels 1 and 8. The average GTG

rise time is 0.75 ms and decay time is 0.79 ms. With such a fast response time, image blur and color breakup can be greatly suppressed.

Figure 12. Simulated voltage-dependent reflectance (VR) curves for RGB of a vertical alignment liquid-crystal-on-silicon (VA LCOS) using UCF-N3 at 50 °C. $d = 0.93 \mu\text{m}$

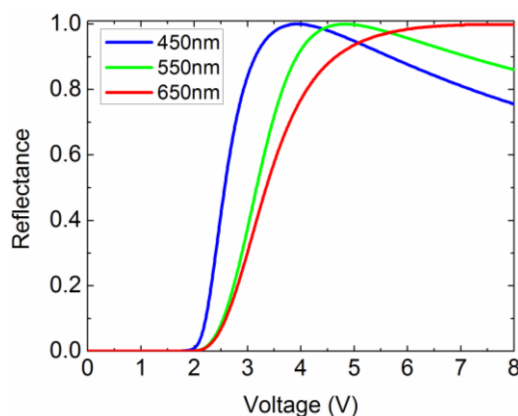


Table 2. Calculated GTG response time (unit: ms) of the UCF-N3 VA LCOS at 50 °C. $d = 0.93 \mu\text{m}$.

		Final Level							
		1	2	3	4	5	6	7	8
Initial Level	–	–	2.36	1.75	1.39	1.13	0.91	0.69	0.26
	1	–	0.34	1.31	1.13	0.95	0.79	0.60	0.22
	2	0.34	–	1.02	0.88	0.73	0.56	0.20	
	3	0.33	1.33	–	0.83	0.69	0.53	0.18	
	4	0.34	1.19	1.03	–	0.68	0.53	0.17	
	5	0.34	1.10	1.01	0.91	–	0.53	0.16	
	6	0.35	1.04	0.98	0.88	0.78	–	0.15	
	7	0.37	1.01	0.96	0.88	0.79	0.68	–	
	8	0.40	1.01	0.97	0.90	0.83	0.74	0.63	–

The estimated operation temperature range for the proposed color sequential VA-LCOS is from 20 °C to 70 °C. As the operation temperature decreases, the response time would be slower because of the increased γ_1/K_{33} . For example, if the application is at room temperature, then from Figure 11a the estimated response time would be ~2.3X slower than that at 50 °C. To shorten response time, overdrive and undershoot voltage method can be applied. On the other hand, if the operation temperature exceeds 70 °C, then the birefringence decreases noticeably as Figure 10 depicts. As a result, the optical efficiency will decline because the phase retardation is less than 1π .

4.1.4. UV Stability

As mentioned above, UV stability is an important concern for an arc-lamp-based LCOS projector. UV light could damage the polyimide alignment layers and the LC material [59]. To investigate UV stability, we exposed our UCF-N3 cell (ITO glass substrates) with a UV LED lamp ($\lambda \sim 385\text{nm}$ and light intensity $\sim 300 \text{ mW/cm}^2$) for five hours. After UV exposure, UCF-N3 shows no sign of

degradation: clearing point, dark state, threshold voltage, and electro-optic properties all remain unchanged within the experimental error.

For a high pressure Mercury arc lamp, the emission spectrum contains some harmful UV components in the 380–400 nm range. Therefore, a UV filter with cutoff wavelength ~ 420 nm is commonly employed. With such a UV filter, our LC mixture should have an excellent stability. For a typical RGB LED backlight unit, its UV content is negligible.

4.1.5. Summary

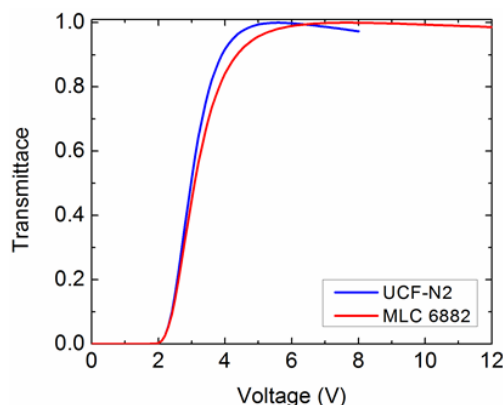
Our fluorinated high birefringence, low viscosity and negative $\Delta\epsilon$ LC mixture UCF-N3 enables a VA LCOS to achieve high contrast ratio, low voltage, and submillisecond GTG response time at an elevated temperature. Such a fast response time enables color sequential display using a single monochrome LCD panel. As a result, the optical system is greatly simplified. Moreover, good UV stability makes this LC mixture practical for projection displays. A thin cell gap ($0.93 \mu\text{m}$) also helps to suppress fringing field effect. Although making a submicron cell gap is technically challenging, it has been done in ferroelectric LCOS devices.

4.2. MVA Mode

For wide-view LCD TVs, MVA [20,60–62] and multi-domain IPS [49,63] are the two major approaches. In a transmissive MVA LCD, the required $d\Delta n$ is 330 nm (at $\lambda = 550 \text{ nm}$) for achieving high transmittance and low driving voltage. The cell gap currently employed is around $3\text{--}4 \mu\text{m}$. Thus, a low viscosity negative $\Delta\epsilon$ LC with $\Delta n \sim 0.08\text{--}0.11$ is commonly used. These LC mixtures are commercially available. For a $3\text{-}\mu\text{m}$ cell gap, the response time is about $4\text{--}5 \text{ ms}$. As the manufacturing technology continues to advance, a thinner cell gap could be used in the near future for reducing response time. For example, if the cell gap can be reduced to $2.5 \mu\text{m}$, then the response time would be improved by $\sim 40\%$, however, the required Δn should be increased to 0.13 . Our low viscosity UCF-N2 ($\Delta n \sim 0.12$) can be considered for MVA applications as well, in addition to n-FFS.

If we keep the cell gap at $3\text{-}\mu\text{m}$ for our UCF-N2, then the on-state voltage is $\sim 5.6 \text{ V}$, as Figure 13 shows. On the other hand, if we use MLC 6882 and keep $d\Delta n = 330 \text{ nm}$ at $\lambda = 550 \text{ nm}$ ($d = 3.37 \mu\text{m}$), then its $V_{\text{on}} \sim 7.6 \text{ V}$. Low voltage helps to reduce power consumption.

Figure 13. Simulated VT curves of two VA cells with UCF-N2 ($d = 3.07 \mu\text{m}$) and MLC 6882 ($d = 3.37 \mu\text{m}$).



5. Conclusions

We have reviewed recent progress on the development of negative $\Delta\epsilon$ LCs for FFS and VA display applications. With our UCF-N2, n-FFS shows superior performance to p-FFS in high transmittance, single gamma curve, cell gap insensitivity, and negligible flexoelectric effect. Using our UCF-N3 for VA LCOS, we have demonstrated a submillisecond gray-to-gray response time for color sequential projection displays. Our low viscosity UCF-N2 can also be used for MVA LCD TVs

Acknowledgments

This work is partially supported by AFOSR under contract No. FA95550-09-1-0170.

Conflicts of Interest

The authors declare no conflict of interest.

References

1. Kirsch, P.; Heckmeier, M.; Tarumi, K. Design and synthesis of nematic liquid crystals with negative dielectric anisotropy. *Liq. Cryst.* **1999**, *26*, 449–452.
2. Kirsch, P.; Reiffenrath, V.; Bremer, M. Nematic liquid crystals with negative dielectric anisotropy: Molecular design and synthesis. *Synlett* **1999**, *1999*, 389–396.
3. Klasen, M.; Bremer, M.; Tarumi, K. New liquid-crystal materials for active matrix displays with negative dielectric anisotropy and low rotational viscosity. *Jpn. J. Appl. Phys.* **2000**, *39*, L1180–L1182.
4. Kirsch, P.; Tarumi, K. A novel type of liquid crystals based on axially fluorinated cyclohexane units. *Angew. Chem. Int. Ed.* **1998**, *37*, 484–489.
5. Schadt, M. Liquid crystal materials and liquid crystal displays. *Annu. Rev. Mater. Sci.* **1997**, *27*, 305–379.
6. Hird, M.; Goodby, J.W.; Toyne, K.J. Nematic materials with negative dielectric anisotropy for display applications. *Proc. SPIE* **2000**, *3955*, 15–23.
7. Ogata, M.; Ukai, K.; Kawai, T. Visual fatigue in congenital nystagmus caused by viewing images of color sequential projectors. *J. Disp. Technol.* **2005**, *1*, 314–320.
8. Chen, Y.; Sun, J.; Xianyu, H.; Wu, S.T.; Liang, X.; Tang, H. High birefringence fluoro-terphenyls for thin-cell-gap TFT-LCDs. *J. Disp. Technol.* **2011**, *7*, 478–481.
9. Hird, M. Fluorinated liquid crystals—Properties and applications. *Chem. Soc. Rev.* **2007**, *36*, 2070–2095.
10. Gray, G.W.; Hird, M.; Toyne, K.J. The synthesis of several lateral difluoro-substituted 4,4''-dialkyl- and 4,4''-alkoxyalkyl-terphenyls and a rationalisation of the effect of such substitution on mesophase type and transition temperatures. *Mol. Cryst. Liq. Cryst.* **1991**, *204*, 43–64.
11. Wu, S.T.; Hsu, C.S.; Chen, J.M. Room temperature difluoro-tolane and diphenyl-diacetylene liquid crystals with negative dielectric anisotropy. *Mol. Cryst. Liq. Cryst.* **1997**, *304*, 441–445.

12. Li, Y.; Chen, Y.; Yan, J.; Liu, Y.; Cui, J.; Wang, Q.; Wu, S.T. Polymer-stabilized blue phase liquid crystal with a negative Kerr constant. *Opt. Mater. Express* **2012**, *2*, 1135–1140.
13. Ge, Z.; Zhu, X.; Wu, T.X.; Wu, S.T. High transmittance in-plane switching liquid crystal displays. *J. Disp. Technol.* **2006**, *2*, 114–120.
14. Oh-e, M.; Kondo, K. Electro-optical characteristics and switching behavior of the in-plane switching mode. *Appl. Phys. Lett.* **1995**, *67*, 3895–3897.
15. Lee, S.H.; Lee, S.L.; Kim, H.Y. Electro-optic characteristics and switching principle of a nematic liquid crystal cell controlled by fringe-field switching. *Appl. Phys. Lett.* **1998**, *73*, 2881–2883.
16. Chen, Y.; Luo, Z.; Peng, F.; Wu, S.T. Fringe-field switching with a negative dielectric anisotropy liquid crystal. *J. Disp. Technol.* **2013**, *9*, 74–77.
17. Yun, H.J.; Jo, M.H.; Jang, I.W.; Lee, S.H.; Ahn, S.H.; Hur, H.J. Achieving high light efficiency and fast response time in fringe field switching mode using a liquid crystal with negative dielectric anisotropy. *Liq. Cryst.* **2012**, *39*, 1141–1148.
18. Schiekkel, M.F.; Fahrenschon, K. Deformation of nematic liquid crystals with vertical orientation in electrical fields. *Appl. Phys. Lett.* **1971**, *19*, 391–393.
19. Kahn, F.J. Electric-field-induced orientational deformation of nematic liquid-crystals: Tunable birefringence. *Appl. Phys. Lett.* **1972**, *20*, 199–201.
20. Takeda, A.; Kataoka, S.; Sasaki, T.; Chida, H.; Tsuda, H.; Ohmuro, K.; Sasabayashi, T.; Koike, Y.; Okamoto, K. A super-high image quality multi-domain vertical alignment LCD by new rubbing-less technology. *SID Symp. Dig. Tech. Pap.* **1998**, *29*, 1077–1080.
21. Ohmuro, K.; Kataoka, S.; Sasaki, T.; Koike, Y. Development of super-high-image-quality vertical-alignment-mode LCD. *SID Int. Symp. Dig. Tech. Pap.* **1997**, *28*, 845–850.
22. Cuypers, D.; De Smet, H.; Van Calster, A. VAN LCOS microdisplays: A decade of technological evolution. *J. Disp. Technol.* **2011**, *7*, 127–134.
23. Khoo, I.C.; Wu, S.T. *Optics and Nonlinear Optics of Liquid Crystals*; World Scientific: Singapore, 1993.
24. Yang, D.K.; Wu, S.T. *Fundamentals of Liquid Crystal Devices*; Wiley: New York, NY, USA, 2006.
25. Wu, S.T.; Wu, C.S. Small angle relaxation of highly deformed nematic liquid crystals. *Appl. Phys. Lett.* **1988**, *53*, 1794–1796.
26. Xu, D.; Rao, L.; Tu, C.-D.; Wu, S.-T. Nematic liquid crystal display with submillisecond grayscale response time. *J. Disp. Technol.* **2013**, *9*, 67–70.
27. Wu, S.T. Nematic liquid crystal modulator with response time less than 100 μ s at room temperature. *Appl. Phys. Lett.* **1990**, *57*, 986–988.
28. Wu, S.T.; Margerum, J.D.; Meng, H.B.; Dalton, L.R.; Hsu, C.S.; Lung, S.H. Room-temperature diphenyl-diacetylene liquid-crystals. *Appl. Phys. Lett.* **1992**, *61*, 630–632.
29. Wu, S.T.; Hsu, C.S.; Shyu, K.F. High birefringence and wide nematic range bis-tolane liquid crystals. *Appl. Phys. Lett.* **1999**, *74*, 344–346.
30. Sekine, C.; Fujisawa, K.; Iwakura, K.; Minai, M. High birefringence phenylacetylene liquid crystals with low viscosity. *Mol. Cryst. Liq. Cryst.* **2001**, *364*, 711–718.
31. Gauza, S.; Jiao, M.; Wu, S.T.; Kula, P.; Dąbrowski, R.; Liang, X. High birefringence and low viscosity negative dielectric anisotropy liquid crystals. *Liq. Cryst.* **2008**, *35*, 1401–1408.

32. Lee, S.H.; Lee, S.M.; Kim, H.Y.; Kim, J.M.; Hong, S.H.; Jeong, Y.H.; Park, C.H.; Choi, Y.J.; Lee, J.Y.; Koh, J.W. Ultra-FFS TFT-LCD with Super Image Quality and Fast Response Time. *SID Symp. Dig. Tech. Pap.* **2001**, *32*, 484–487.
33. Lee, S.H.; Lee, S.L.; Kim, H.Y.; Eom, T.Y. A novel wide-viewing-angle technology: Ultra-Trans View™. *SID Symp. Dig. Tech. Pap.* **1999**, *30*, 202–205.
34. Blinov, L.M.; Chigrinov, V.G. *Electrooptic Effects in Liquid Crystal Materials*; Springer-Verlag: New York, NY, USA, 1994.
35. Lee, J.H.; Park, K.H.; Kim, S.H.; Choi, H.C.; Kim, B.K.; Yin, Y. AH-IPS: Superb display for mobile device. *SID Symp. Dig. Tech. Pap.* **2013**, *44*, 32–33.
36. Wen, C.H.; Gauza, S.; Wu, S.T. High-contrast vertical alignment of lateral difluoro-terphenyl liquid crystals. *Appl. Phys. Lett.* **2005**, *87*, 191909:1–191909:3.
37. Clark, M.G.; Raynes, E.P.; Smith, R.A.; Tough, R.J.A. Measurement of the permittivity of nematic liquid-crystals in magnetic and electric-fields using extrapolation procedures. *J. Phys. D Appl. Phys.* **1980**, *13*, 2151:1–2151:11.
38. Wu, S.T.; Wu, C.S. Experimental confirmation of the Osipov-Terentjev theory on the viscosity of nematic liquid-crystals. *Phys. Rev. A* **1990**, *42*, 2219–2227.
39. Wu, S.T.; Efron, U.; Hess, L.D. Birefringence measurements of liquid-crystals. *Appl. Opt.* **1984**, *23*, 3911–3915.
40. Haller, I. Thermodynamic and static properties of liquid crystals. *Prog. Solid State Chem.* **1975**, *10*, 103–118.
41. Wu, S.T. Birefringence dispersions of liquid-crystals. *Phys. Rev. A* **1986**, *33*, 1270–1274.
42. Wu, S.T.; Lackner, A.M.; Efron, U. Optimal operation temperature of liquid-crystal modulators. *Appl. Opt.* **1987**, *26*, 3441–3445.
43. Lien, A. Extended Jones Matrix representation for the twisted nematic liquid-crystal display at oblique-incidence. *Appl. Phys. Lett.* **1990**, *57*, 2767–2769.
44. Ge, Z.B.; Wu, S.T.; Kim, S.S.; Park, J.W.; Lee, S.H. Thin cell fringe-field-switching liquid crystal display with a chiral dopant. *Appl. Phys. Lett.* **2008**, *92*, 181109:1–181109:3.
45. Hong, S.H.; Park, I.C.; Kim, H.Y.; Lee, S.H. Electro-optic characteristic of fringe-field switching mode depending on rubbing direction. *Jpn. J. Appl. Phys.* **2000**, *39*, L527–L530.
46. Sun, Y.; Zhang, Z.; Ma, H.; Zhu, X.; Wu, S.T. Optimal rubbing angle for reflective in-plane-switching liquid crystal displays. *Appl. Phys. Lett.* **2002**, *81*, 4907–4909.
47. Jiao, M.; Ge, Z.; Song, Q.; Wu, S.T. Alignment layer effects on thin liquid crystal cells. *Appl. Phys. Lett.* **2008**, *92*, 061102:1–061102:3.
48. Hatsumi, R.; Kubota, Y.; Moriya, K.; Kubota, D.; Tanabe, T.; Kusunoki, K.; Hirakata, Y.; Koyama, J.; Yamazaki, S.; Nakamura, A.; Chubachi, Y. Driving method of FFS-Mode OS-LCD for reducing eye strain. *SID Symp. Dig. Tech. Pap.* **2013**, *44*, 338–341.
49. Lu, R.; Zhu, X.; Wu, S.T.; Hong, Q.; Wu, T.X. Ultrawide-view liquid crystal displays. *J. Disp. Technol.* **2005**, *1*, 3–14.
50. Zhu, X.; Ge, Z.; Wu, S.T. Analytical solutions for uniaxial-film-compensated wide-view liquid crystal displays. *J. Disp. Technol.* **2006**, *2*, 2–20.
51. Armitage, D.; Underwood, I.; Wu, S.T. *Introduction to Microdisplay*; Wiley: Hoboken, NJ, USA, 2006.

52. Brennesholtz, M.S.; Stupp, E.H. *Projection Displays*; Wiley: Chichester, UK, 2008.
53. Gauza, S.; Zhu, X.; Piecek, W.; Dabrowski, R.; Wu, S.T. Fast switching liquid crystals for color-sequential LCDs. *J. Disp. Technol.* **2007**, *3*, 250–252.
54. Wu, S.T.; Wu, C.S. Mixed-mode twisted nematic liquid crystal cells for reflective displays. *Appl. Phys. Lett.* **1996**, *68*, 1455–1457.
55. Lee, S.; Mao, C.C.; Johnson, K.M. Fast-switching liquid-crystal-on-silicon microdisplay with Framebuffer pixels and surface-mode optically compensated birefringence. *Opt. Eng.* **2006**, *45*, 127402:1–127402:8.
56. Fan-Chiang, K.H.; Wu, S.T.; Chen, S.H. Fringing-field effects on high-resolution liquid crystal microdisplays. *J. Disp. Technol.* **2005**, *1*, 304–313.
57. Wang, H.; Wu, T.X.; Zhu, X.; Wu, S.T. Correlations between liquid crystal director reorientation and optical response time of a homeotropic cell. *J. Appl. Phys.* **2004**, *95*, 5502–5508.
58. Chen, Y.; Peng, F.; Wu, S.T. Submillisecond-response vertical-aligned liquid crystal for color sequential projection displays. *J. Disp. Technol.* **2013**, *9*, 78–81.
59. Wen, C.H.; Gauza, S.; Wu, S.T. Photostability of liquid crystals and alignment layers. *J. Soc. Inf. Disp.* **2005**, *13*, 805–811.
60. Kim, S.S. The world's largest (82-in) TFT-LCD. *SID Symp. Dig. Tech. Pap.* **2005**, *36*, 1842–1847.
61. Miyachi, K.; Kobayashi, K.; Yamada, Y.; Mizushima, S. The world's first photo alignment LCD technology applied to Generation Ten factory. *SID Symp. Dig. Tech. Pap.* **2010**, *41*, 579–582.
62. Lee, S.H.; Kim, S.M.; Wu, S.T. Emerging vertical-alignment liquid-crystal technology associated with surface modification using UV-curable monomer. *J. Soc. Inf. Disp.* **2009**, *17*, 551–559.
63. Hong, H.; Shin, H.; Chung, I. In-plane switching technology for liquid crystal display television. *J. Disp. Technol.* **2007**, *3*, 361–370.

© 2013 by the authors; licensee MDPI, Basel, Switzerland. This article is an open access article distributed under the terms and conditions of the Creative Commons Attribution license (<http://creativecommons.org/licenses/by/3.0/>).